On the 3-D inverse potential target pressure problem. Part 2. Numerical aspects and application to duct design

By V. DEDOUSSIS[1,2], P. CHAVIAROPOULOS[1]
AND K. D. PAPAILIOU[1]

[1] National Technical University of Athens, Laboratory of Thermal Turbomachines,
PO Box 64069, 157 10 Athens, Greece

[2] Department of Industrial Management, University of Piraeus, 185 34 Piraeus, Greece

A potential function/stream function formulation is introduced for the solution of the fully 3-D inverse potential 'target pressure' problem. In the companion paper (Part 1) it is seen that the general 3-D inverse problem is ill-posed but accepts as a particular solution elementary streamtubes with orthogonal cross-section. Under this simplification, a novel set of flow equations was derived and discussed. The purpose of the present paper is to present the computational techniques used for the numerical integration of the flow and geometry equations proposed in Part 1. The governing flow equations are discretized with centred finite difference schemes on a staggered grid and solved in their linearized form using the preconditioned GMRES algorithm. The geometry equations which form a set of first-order o.d.e.s are integrated numerically using a second-order-accurate space marching scheme. The resulting computational algorithm is applied to a double turning duct and a 3-D converging–diverging nozzle 'reproduction' test case.

1. Introduction

In the companion paper, Part 1 (Chaviaropoulos, Dedoussis & Papailiou 1995), a 'single-pass' inverse potential method for the solution of the three-dimensional (3-D) 'target pressure' problem has been developed. Similar to the approach proposed by Stanitz (1980, 1985), a potential function ϕ and two stream functions ψ, η are introduced as the 'natural' coordinates. A body-fitted coordinate transformation is employed to map the physical (x, y, z)-space on which the boundaries of the flow field are unknown onto the natural (ϕ, ψ, η)-space. The governing flow equations are derived using the metrics compatibility conditions of the 3-D Euclidean (flat) space. A novel closed set of three partial differential equations (p.d.e.s) is, thus, derived in terms of the velocity magnitude V, and the aspect ratio t and the skew angle θ of the elementary streamtube cross-section. Because of the nature of the governing V–t–θ equations, the 3-D inverse problem with velocity (pressure)-only boundary conditions does not have a unique solution. The problem, however, accepts as a particular solution elementary streamtubes with orthogonal cross-sections. In this case, the governing flow equations simplify to an elliptic-type p.d.e. for the velocity magnitude and to a second-order o.d.e. for the streamtube aspect ratio. The solution of these two equations provides the flow field in a 'single-pass' manner without requiring any feedback from the geometry. The geometry is determined in a subsequent step by integrating Frenet equations along the natural coordinates lines.

The purpose of this paper, Part 2 of the study, is to present the numerical implementation of the 3-D inverse design method developed in Part 1. The governing flow equations are discretized on the (ϕ, ψ, η)-space using centred finite differencing. A staggered $V-t$ computational stencil is employed in order to enhance the accuracy of the discretization in the near-boundary regions. The resulting discrete system of equations is linearized to form a Newton iteration step. The explicit Jacobian inversion in the Newton step is avoided by employing a fast iterative linear system solver, based on the preconditioned restarting GMRES(m) algorithm (Saad & Schultz 1983). An incomplete L–U preconditioner, resulting from the MSIP approximate factorization scheme (Zedan & Schneider 1983), premultiplies the velocity block of the Jacobian matrix, while tridiagonal preconditioning is applied to the t-block of the Jacobian matrix.

Once the flow field has been determined, the geometry is calculated by integrating Frenet equations along the (ϕ, ψ, η)-coordinate lines. Frenet equations form coupled systems of o.d.e.s expressing the variation of the covariant base $(\boldsymbol{g}_1, \boldsymbol{g}_2, \boldsymbol{g}_3)$ and the position vector $\boldsymbol{r}$ along the natural coordinates lines. In order to enhance the accuracy of the discretization, a staggered computational stencil is also employed. A Crank–Nicholson-type second-order-accurate space marching scheme is used for the numerical integration of the discrete equations.

The method is validated in the last part of the paper for two channel flow 'reproduction' test cases, concerning a double turning converging duct and an axial 3-D converging–diverging nozzle.

2. Governing equations

Assuming that the flow is steady inviscid and irrotational and that the fluid is a perfect gas, the velocity field may be expressed as the gradient of a potential function ϕ, and the flux field as the cross-product of two stream function (ψ, η) gradients (Yih 1957). Thus

$$V = \nabla\phi, \tag{1}$$

$$\rho V = \nabla\psi \times \nabla\eta. \tag{2}$$

The density field is related to the velocity magnitude through the energy conservation equation for isentropic changes as

$$\rho = \left[1 + \frac{\gamma - 1}{2} M_\infty^2 (1 - V^2)\right]^{1/(\gamma - 1)}. \tag{3}$$

In the above equations the velocity V is normalized with a reference value V_∞ and the density ρ with the corresponding ρ_∞ value. M_∞ is the Mach number at the reference point and γ is the ratio of specific heats c_p/c_v.

2.1. *Flow equations*

Considering the coordinate transformation of the physical (x, y, z)-space onto the natural (ϕ, ψ, η) one, the governing equations of the inverse problem are derived from the metrics compatibility (zero-curvature) conditions on the natural space. Under the assumption of orthogonal streamtubes the velocity and streamtube aspect ratio (Part 1) dependent variables satisfy the following p.d.e.s in the natural coordinates space:

velocity (V) equation

$$(\ln V)_{\phi\phi} + (\ln \rho)_{\phi\phi} + (\rho t/V)(\ln V)_{\psi\psi} + (\rho/tV)(\ln V)_{\eta\eta} + \tfrac{1}{2}[(\ln V)_\phi^2 - (\ln t)_\phi^2 - (\ln \rho)_\phi^2]$$
$$- (\rho t/V)(\ln V)_\psi[(\ln V)_\psi - (\ln t)_\psi] - (\rho/tV)(\ln V)_\eta[(\ln V)_\eta + (\ln t)_\eta] = 0; \tag{4}$$

aspect ratio (*t*) equation

$$(\ln t)_{\phi\phi} - (\ln \rho)_\phi (\ln t)_\phi + (\rho t/V)[(\ln V)_{\psi\psi} + (\ln V)_\psi (\ln \rho)_\psi]$$
$$- (\rho/tV)[(\ln V)_{\eta\eta} + (\ln V)_\eta (\ln \rho)_\eta] = 0, \quad (5)$$

where subscripts ϕ, ψ, η indicate corresponding partial derivatives. The above set of equations supplemented by the density equation (3) form a closed set of p.d.e.s for the dependent flow variables, i.e. the velocity magnitude V, the streamtube aspect ratio t and the density ρ.

As it is pointed out in Part 1, in subsonic flows and for a given t-field, (4) represents an elliptic quasi-linear p.d.e. for $(\ln V)$, requiring boundary conditions all around the integration domain. In the context of the present work, where internal configurations are considered, velocity is specified (Dirichlet-type conditions) on the limiting lateral stream surfaces (walls), either as $V = V(\phi, \psi)|_{\eta=\text{const}}$ or $V = V(\phi, \eta)|_{\psi=\text{const}}$ and on the inlet and outlet sections, which are assumed to be potential surfaces, as $V = V(\psi, \eta)|_{\phi=\text{const}}$. On the solid walls potential ϕ is related to streamline arclength s via the relation $d\phi = V ds$. It is obvious, therefore, that $V = V(\phi, \psi)|_{\eta=\text{const}}$, for instance, could be considered as $V = V(s, \psi)|_{\eta=\text{const}}$. The designer usually specifies the distribution $V = V(s)$ rather than $V = V(\phi)$.

For a given V-field, t-equation (5) is a second-order, o.d.e. for $(\ln t)$ in the ϕ-wise sense. Considering the t-equation as a boundary value problem, boundary conditions are required both on the inlet and outlet sections. Dirichlet-type boundary conditions are imposed on the inlet section, the actual value depending on the ψ–η discretization (e.g. $t = 1$ for $\Delta\psi = \Delta\eta$). Assuming that the flow on the outlet section is 'non-evolving', i.e. fully developed, a zero Neumann boundary condition is specified there.

The way the boundary conditions for both V and t are implemented implicitly assumes that an H-type partitioning for the (ψ, η)-plane, i.e. cross-sections, has been employed. According to the discussion presented in Part 1, the H-type partitioning in conjunction with the assumption of orthogonal streamtubes, restrict the application of the method to the design of geometries with orthogonally edged lateral boundaries. It has been pointed out, however, that a possible more flexible O-type partitioning would require additional boundary conditions along the singular streamline. For simplicity H-type partitioning has been adopted in this work.

In contrast to the 2-D case, the 3-D set of flow equations (4) and (5) is strongly nonlinear even for the simplest case, the incompressible one. In that respect, the present 3-D formulation cannot be considered as a straightforward extension of the 2-D theory. However, the very important similarity is that in both the 2-D and 3-D formulations the flow field can be determined without any feedback from the geometry sought. The present potential function/stream function inverse approach represents, therefore, a fast, 'single-pass', design method.

2.2. Geometry equations

Having determined the flow field in the (ϕ, ψ, η)-space, the relevant geometry is computed by integrating the Frenet equations along the coordinate lines of the natural space. The Frenet equations which govern the variation of the covariant base and, consequently, the position vector r along the $\phi = $ const., $\psi = $ const. and $\eta = $ const. lines form a coupled system of o.d.e.s. In compact tensor notation this system reads

$$\frac{\partial \mathbf{g}_i}{\partial u^j} = \Gamma_{ij}^k \mathbf{g}_k \quad \text{with} \quad i, j, k = 1, 2, 3, \quad (6)$$

where
$$g_i = \frac{\partial r}{\partial u^i}, \quad (u^1, u^2, u^3) \equiv (\phi, \psi, \eta). \tag{7}$$

As has been pointed out in Part 1, the Christoffel symbols Γ^k_{ij} are expressed analytically in terms of the partial derivatives of the flow field quantities, V, t and ρ.

Equation (6) represents a 3×3 system of scalar o.d.e.s along the natural coordinate direction u^i for each of the Cartesian components of the covariant base (g_1, g_2, g_3). Once the covariant base components become available, the integration of (7) provides the Cartesian coordinates of the geometry. To integrate (6) and (7), the orthogonal covariant base and the position vector should be arbitrarily specified at a reference point, say the centroid of the inlet section.

3. Numerical integration of flow equations

The objective of this section is to discuss in detail the discretization, the linearization and the iterative solver employed for the numerical integration of the system of flow equations (4) and (5).

3.1. Discretization

Here $(\ln V)$ and $(\ln t)$ are considered to be the dependent computational variables. First- and second-order partial derivatives are discretized using second-order-accurate central differencing on a uniform (ϕ, ψ, η)-grid. Derivatives of $(\ln \rho)$ are directly related to the $(\ln V)$ derivatives through (3).

On the cross-flow plane the discretization of the equations has been effected on a staggered grid: t-nodes are off-set with respect to the V- and ρ-nodes, which are considered to be the actual grid nodes, by half a cell distance, both in the ψ- and η-directions. Namely, if I, J and K indices are associated with the grid nodes in the ϕ-, ψ- and η-directions respectively, then V and ρ are stored at (I, J, K) locations, whilst t is stored at $(I, J+\frac{1}{2}, K+\frac{1}{2})$ locations (see figure 1).

The advantage of this staggering is twofold. From the numerical point of view, the first-order cross-flow derivatives of $(\ln V)$ and $(\ln t)$ are tightly coupled. At mid-cell locations, $(\ln V)$ and $(\ln t)$ cross-flow derivatives are approximated assuming linear variation within the cells. For example

$$[(\ln V)_\psi]_{I, J+\frac{1}{2}, K+\frac{1}{2}} = \frac{1}{2\Delta\psi}[(\ln V)_{I, J+1, K+1} - (\ln V)_{I, J, K+1}$$
$$+ (\ln V)_{I, J+1, K} - (\ln V)_{I, J, K}]. \tag{8}$$

This implies that there is no need for one-sided differencing on the boundary cells for the discretization of $(\ln V)_\psi$ and $(\ln V)_\eta$ contained in the t-equation (5). The required mid-cells values, $V_{I, J+\frac{1}{2}, K+\frac{1}{2}}$ for the t-equation and $t_{I, J, K}$ for the V-equation (4) are approximated assuming linear variation of $(\ln V)$ and $(\ln t)$ in the corresponding cell. The definition of t as the elementary streamtube aspect ratio, on the other hand, requires t to be stored at the centroid of the streamtube cross-section. In that respect, the adopted staggering practice is also physically sound.

The central differencing for the V-equation limits the present approach to subsonic flows only, where the equation is elliptic. In the case of transonic flow, upwind differencing in the streamwise ϕ-direction should be used.

3.2. Linearization

The V- and t-equations are highly nonlinear and have different mathematical characters. It has been decided, therefore, to solve them in a coupled iterative mode. A
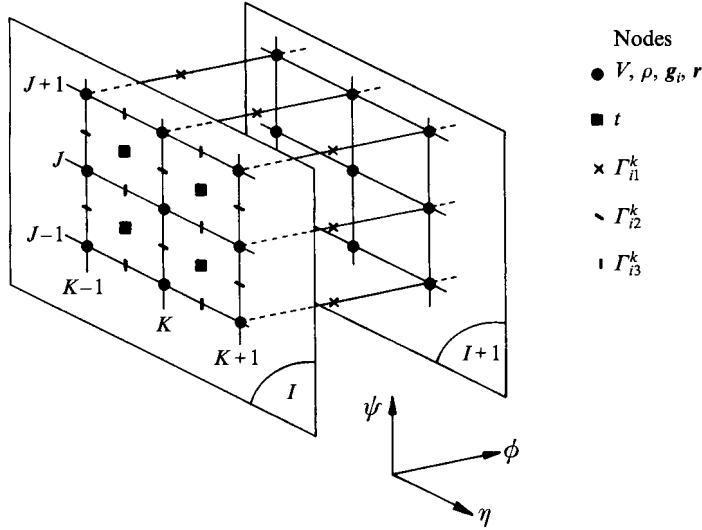
FIGURE 1. Staggered computational stencil for the flow field and geometry calculations.

Newton procedure, where nonlinear terms are expanded in the iteration space using Taylor series, is employed to linearize the discrete system of equations. This linearization procedure results to the following iteration:

$$0 = R^{n+1} = R^n + \left[\frac{\partial R}{\partial X}\right]^n \Delta X, \tag{9}$$

$$X^{n+1} = X^n + \Delta X; \quad X = \begin{bmatrix} \ln V \\ \ln t \end{bmatrix}, \tag{10}$$

where superscript n denotes the iteration level and R is the residual vector of the V and t-system of equations.

In writing the linearization relation (9), the dependence of the governing equation on ρ is not shown explicitly. This is because ρ is frozen during the (V, t) iteration (a practice which is very common in subsonic flow computations). The density field is updated after $(V, t)^{n+1}$ have been determined, using the algebraic equation (3).

3.3. *Solution algorithm*

The solution of the discrete block system of (9) is carried out using an iterative technique based on a preconditioned gradient method. Preconditioning is essential since matrix $(\partial R / \partial X)$ is stiff. The most obvious choice for the preconditioning matrix P is

$$P \sim \left[\frac{\partial R}{\partial X}\right]^{-1}. \tag{11}$$

Indicating the dependence of $(\partial R / \partial X)$ on the unknowns V and t this Jacobian matrix can be expressed in terms of corresponding submatrices as

$$\frac{\partial R}{\partial X} = \begin{bmatrix} L_1 & L_2 \\ L_3 & L_4 \end{bmatrix}. \tag{12}$$

Neglecting the effect of submatrix L_2, a preconditioning matrix may be obtained in the form:

$$P = \begin{bmatrix} P_1 & 0 \\ P_3 & P_4 \end{bmatrix}, \tag{13}$$

where $\qquad P_1 \sim L_1^{-1}, \quad P_4 \sim L_4^{-1}, \quad P_3 \sim -L_4^{-1}L_3L_1^{-1} \sim -P_4L_3P_1.$ (14)

In its discrete form P_1 is derived by an incomplete L–U decomposition of L_1 using the MSIP technique (Zedan & Schneider 1983). P_4 is approximated by

$$P_4 = \left[\frac{I}{\Delta\tau} + L_4\right]^{-1}.$$ (15)

Operator P_4 is related to the inversion of a tridiagonal matrix since L_4, which expresses the dependence of the *t*-equation on $(\ln t)$, is a one-dimensional three-point discrete operator. The pseudo-time term $(I/\Delta\tau)$ serves as a relaxation parameter, while its positive sign contributes to the diagonal dominance of the tridiagonal matrix. Appropriate values of $\Delta\tau$ have been determined via computational experimentation.

The preconditioned form of the Newton step, i.e. (9) premultiplied by the P matrix, is solved with the linear, restarting GMRES (m) algorithm (Saad & Schultz 1983), which has been proved to be very effective in a wide variety of CFD problems (Giannakoglou, Chaviaropoulos & Papailiou 1988).

4. Numerical integration of geometry equations

The calculation of the geometry which exhibits the prescribed flow properties is the objective of an inverse method. In that sense the numerical schemes which are used for the integration of the geometry equations should be very accurate. Compared to the inner-flow region the calculation of the lateral boundaries is more demanding, because the required flow information is not completely available there. This effect is more pronounced on the edges (intersections of the limiting stream surfaces of different family) where the ψ and η surface derivatives are discontinuous. To circumvent this difficulty staggered grid techniques have been employed. Details of the discretization and integration procedure of the geometry equations are discussed in this section.

4.1. *Discretization*

The covariant base (g_1, g_2, g_3) is computed on the actual grid nodes (I, J, K) which are V- and ρ-nodes. Depending on the direction of the integration of (6), the corresponding Christoffel symbols appearing in its right-hand side are stored at different locations. Noting that the Christoffel symbols are expressed in terms of the first-order derivatives of the flow quantities (V, t, ρ), the staggering to be adopted should be such that the discrete form of these derivatives use inner-grid information, avoiding as much as possible variables extrapolation. Thus, the Γ_{i1}^k Christoffel symbols, which are associated with the streamwise ϕ-direction of the covariant base integration, are calculated at $(I+\frac{1}{2}, J, K)$ locations. Accordingly, the Γ_{i2}^k and Γ_{i3}^k symbols, associated with the ψ- and η-integrations respectively, are calculated at $(I, J+\frac{1}{2}, K)$ and $(I, J, K+\frac{1}{2})$ locations respectively (see figure 1). It is noted that the assumptions adopted for the variation of the flow variables in the grid cells are also used in the actual evaluation of the Γ_{ij}^k symbols.

4.2. *Solution algorithm*

The numerical integration of the geometry equations (6) and (7) is performed in two steps. First, the covariant base g_i is determined applying an implicit second-order-accurate Crank–Nikolson scheme along the natural coordinates. Along the streamwise coordinate, for instance, the discrete form of (6) reads

$$\frac{G_{I+1,J,K} - G_{I,J,K}}{\Delta\phi} = A_{\phi_{I+\frac{1}{2},J,K}} \tfrac{1}{2}\{G_{I+1,J,K} + G_{I,J,K}\},$$ (16)

or, dropping the cross-plane indices

$$G_{I+1} - G_I = \tfrac{1}{2}\Delta\phi A_{\phi_{I+\frac{1}{2}}}\{G_{I+1} + G_I\}, \tag{17}$$

where
$$G = \begin{bmatrix} g_1 \\ g_2 \\ g_3 \end{bmatrix} = \begin{bmatrix} g_{1x} & g_{1y} & g_{1z} \\ g_{2x} & g_{2y} & g_{2z} \\ g_{3x} & g_{3y} & g_{3z} \end{bmatrix} \quad \text{and} \quad A_\phi = \begin{bmatrix} \Gamma_{11}^1 & \Gamma_{11}^2 & \Gamma_{11}^3 \\ \Gamma_{21}^1 & \Gamma_{21}^2 & \Gamma_{21}^3 \\ \Gamma_{31}^1 & \Gamma_{31}^2 & \Gamma_{31}^3 \end{bmatrix}, \tag{18}$$

with x, y, z indices indicating the corresponding Cartesian components. Quantities appearing in (16) and (17) are compatible with the discretization strategy presented in the previous subsection. Assuming that G_I is known, G_{I+1} is provided through

$$G_{I+1} = \{I - \tfrac{1}{2}\Delta\phi A_{\phi_{I+\frac{1}{2}}}\}^{-1}\{I + \tfrac{1}{2}\Delta\phi A_{\phi_{I+\frac{1}{2}}}\} G_I, \tag{19}$$

with I being the 3×3 identity matrix. Equations similar to (19) hold for the ψ and η integrations.

To determine the covariant base distribution on the complete grid, (19) is first applied to the centreline. The integration of (19) starts from the inlet section on which the orientation of the orthogonal covariant base is arbitrarily specified, its size being controlled by the corresponding metrics which in turn are expressions of the V and t boundary distributions. On each cross-flow plane, i.e. potential (ϕ = const.) surface, G is determined via a combination of ψ- and η-integrations. Starting from the calculated covariant base on the central grid node (centreline distribution), two ψ-integrations (in the positive and negative sense) are carried out in order to determine the G-distribution along the central η-family grid line. This latter distribution provides the initial conditions for the η-integrations which are carried out along all ψ-family grid lines. Obviously, the order of ψ- and η-integrations performed for the calculation of the G-distribution on the cross-flow plane may be interchanged. An averaging practice has been adopted in this work. In duct flow applications the above directional integration scheme was found to be the most effective in terms of minimal error accumulation.

Having calculated the G-field, the geometry is determined by straightforward second-order-accurate numerical integrations of (7) along the (ϕ, ψ, η)-grid following a similar directional integration strategy. On the cross-flow plane (ϕ = const. surfaces) for instance, the ψ- and η-integrations read respectively

$$r_{I,J+1,K} = r_{I,J,K} + \Delta\psi \tfrac{1}{2}\{g_{2_{I,J+1,K}} + g_{2_{I,J,K}}\}, \tag{20}$$

$$r_{I,J,K+1} = r_{I,J,K} + \Delta\eta \tfrac{1}{2}\{g_{3_{I,J,K+1}} + g_{3_{I,J,K}}\}. \tag{21}$$

In accordance with the scheme used for the covariant base calculation, the sought geometry at (I, J, K) locations, i.e. the position vector $r_{I,J,K}$, is finally obtained with straightforward averaging.

The magnitude of the covariant base vectors is directly related to the metrics (note that $g_i \cdot g_i = (g_i)^2 = g_{ii}$, repeated indices are not summed here). The metrics, on the other hand, are expressed in terms of the flow quantities V, t and ρ. It is evident that the covariant base vectors, calculated via the numerical integration of the geometry equations (6) and (7) should be compatible with (the already known) corresponding metrics. Stanitz (1985) found it necessary to incorporate a magnitude correction within the geometry calculation procedure, so as to ensure compatibility between the geometry and the flow field (a direction correction for the base vectors was also incorporated). The velocity equation, that Stanitz (1980, 1985) used, has coefficients which are explicit functions of geometric parameters. It seems that corrections are necessary to minimize possible adverse (nonlinear) feedback of geometry errors, within

the overall calculation procedure. In our method and for the design test cases attempted it was not necessary to cater for any geometry correction technique. Perhaps, this is due to the principal characteristic of the proposed 3-D inverse method that the flow and geometry calculation procedures are decoupled, i.e. they are entirely independent.

5. Results and discussion

The method has been validated for two channel-flow 'reproduction' test cases. In the first case a direct full-potential code is employed in order to provide the flow field in a double turning converging duct. The computed boundary velocity distributions form the input data for the inverse solver which is called upon to reproduce the original geometry. The opposite procedure is followed in the second test case where an axial 3-D converging–diverging nozzle is designed. In this case, the inverse solver provides a geometry compatible with a prescribed 'target pressure' and the direct solver is called upon to produce the prescribed boundary velocity (pressure) distribution. These 'reproduction' cases form a hard test for the accuracy of both the inverse and direct solvers since the numerical errors tend to accumulate within the two-step validation procedure.

5.1. *Double turning duct test case*

This case concerns the reproduction of a 3-D subsonic, double turning converging duct. The geometry of the duct, which is shown in figure 2(*a*), has been defined analytically (Workshop on Selected Inverse and Optimum Design Problems, organized by Brite Euram Project 1082 partners, June 1992). Inlet Mach number is set to 0.2, leading to a high subsonic exit Mach number of the order of 0.75.

A full-potential 3-D solver (Chaviaropoulos, Giannakoglou & Papailiou 1988) is employed to obtain the flow field and the velocity distribution on the lateral walls of the duct. The wall (as well as the inlet and outlet) velocity distributions calculated by the direct solver are used as input by the 3-D inverse method in order to reproduce the geometry of the duct. The 3-D inverse solver, however, requires the velocity distributions along the boundary (limiting) streamlines which, in general, do not coincide with the boundary grid lines of the direct solver. One has, therefore, to translate the flow field calculated by the direct code to a form which can be comprehended by the inverse method. For this purpose a post-processor has been developed, which performs the following tasks:

(i) Assuming that streamsurfaces (i.e. $\psi = $ const., $\eta = $ const. lines) are uniformly distributed at the inlet plane, a streamline computation is carried out. The procedure is based on the integration of the following transport equations:

$$V \cdot \nabla \psi = 0, \quad V \cdot \nabla \eta = 0, \tag{22}$$

where V is the velocity (vector) field calculated by the direct solver. Boundary conditions for ψ and η are required on the inlet plane only. The numerical integration of these two transport-type equations is performed employing an upwind approximate factorization scheme (Rao, Steger & Pletcher 1987) using the values of the potential ϕ and stream functions ψ, η at the grid nodes of the original geometry.

(ii) Respecting the limiting values of the ϕ, ψ, η independent variables a uniform rectangular computational grid is generated on the (ϕ, ψ, η)-space.

(iii) The velocity magnitude is then determined on the grid nodes of the computational (ϕ, ψ, η)-space (which do not coincide with the original geometry grid
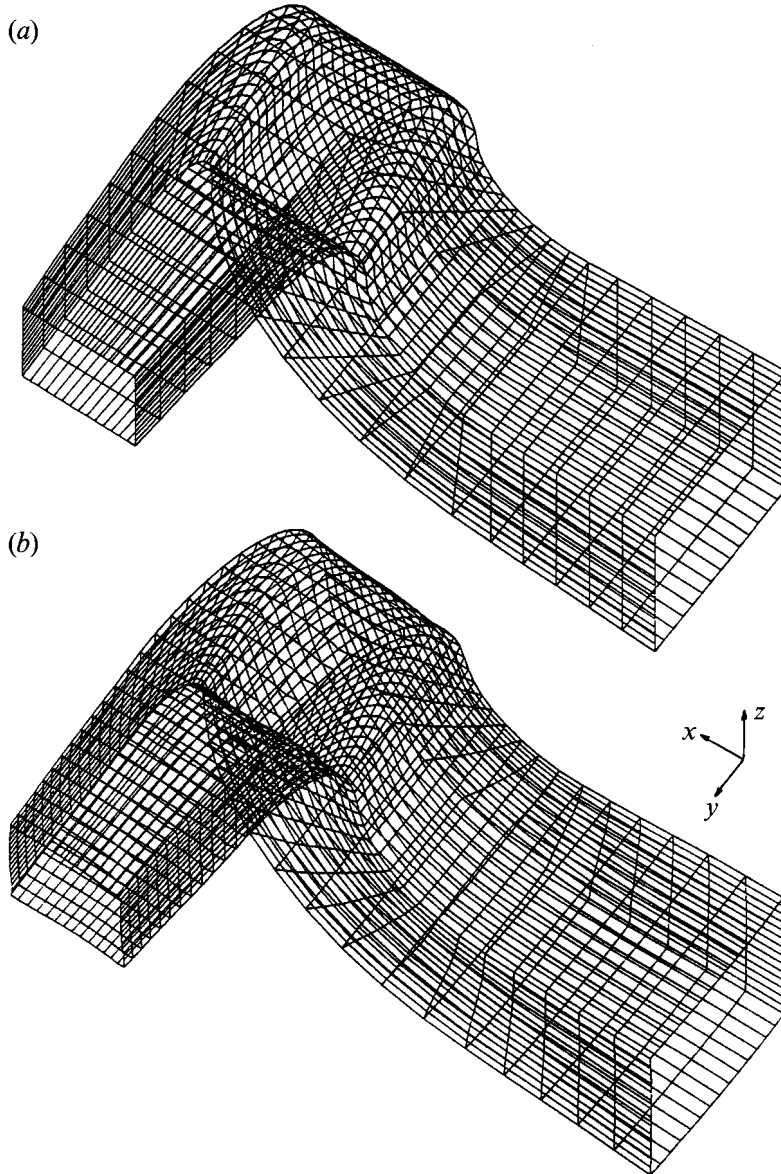
(a)

(b)

FIGURE 2. Perspective views of (a) the original and (b) the reproduced double turning duct.

nodes). A second-order-accurate interpolation procedure, using Taylor series expansion, is used for this purpose.

Clearly, one expects that the numerical errors accumulated in this interpolation procedure affect to some extent the accuracy of the 'reproduction'. To minimize the numerical errors involved, a relatively fine ($30 \times 15 \times 15$) computational grid was used in the direct computation.

A $43 \times 15 \times 15$ unifom grid was generated on the (ϕ, ψ, η)-space. The computational cost associated with the inverse problem solution is of the order of 650 CPU s in one processor of an Alliant FX 80 computer. A representative view of the original and reproduced duct geometries is presented in figures 2(a) and 2(b) respectively, while projections of the corresponding centrelines on the (x, z)- and (y, z)-planes are
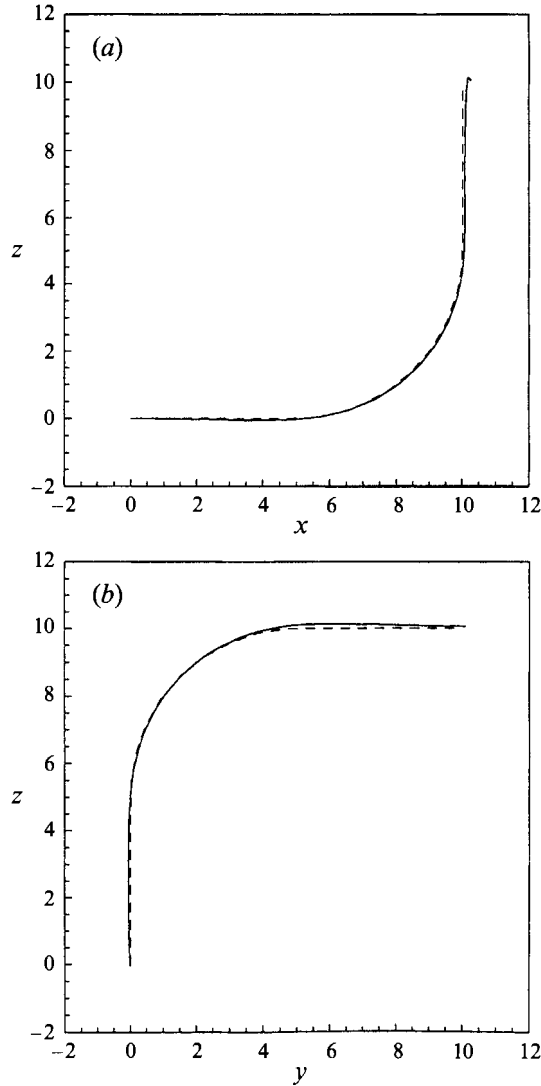
FIGURE 3. Projections of the centreline of the original (----) and the reproduced (——) double turning duct on (*a*) the (*x*, *z*)- and (*b*) on the (*y*, *z*)-plane.

compared in figures 3(*a*) and 3(*b*). It should be noted that the centreline of the reproduced geometry is not a direct output of the inverse method. Its geometry is determined by averaging the calculated Cartesian coordinates of the four streamline edges. This practice is acceptable since the duct under discussion has square cross-section. The satisfactory comparisons of both the centreline and the lateral wall geometries indicate the accuracy of the proposed 3-D inverse method. Inevitably, some discrepancies are introduced by the interpolations and the different discretization schemes which are used in the direct and inverse solvers. Small discrepancies of the geometry near the edges of the duct are due to the singular behaviour of the corresponding streamlines.

Mach number distributions calculated with the inverse and direct solvers along the centreline of the duct are compared in figure 4. As the flow proceeds downstream, the
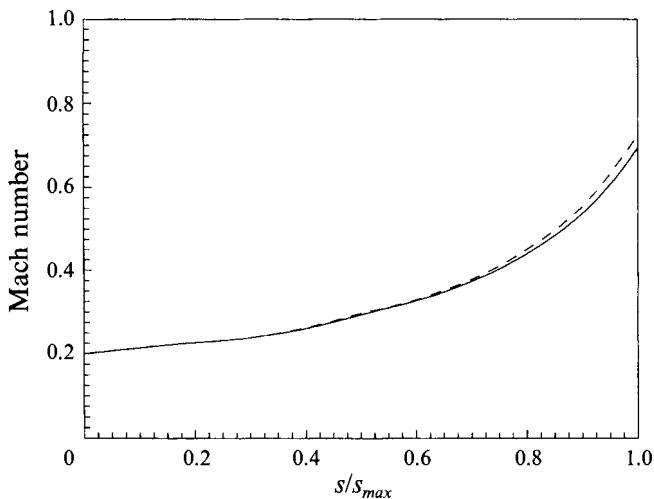
FIGURE 4. Mach number distributions along the centreline of the double turning duct: ———, inverse solution; — — —, direct solution, original geometry.
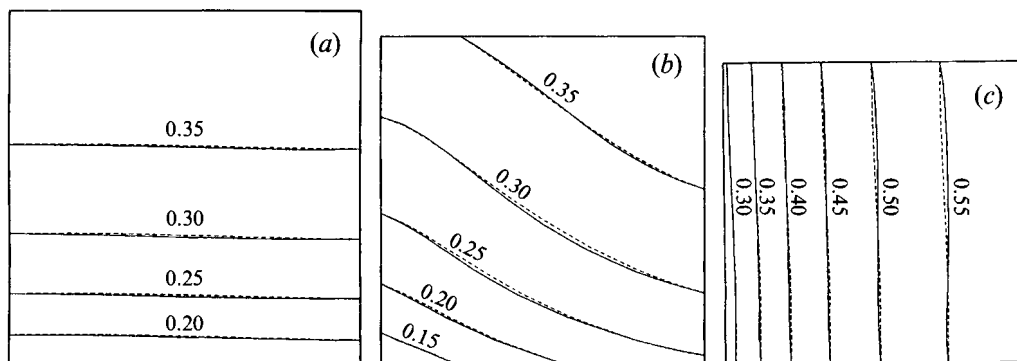

FIGURE 5. Mach number contours of inverse (———) and direct (— — —) method on sections normal to the centreline of the double turning duct at (*a*) $s = \frac{1}{3}s_{max}$, (*b*) $s = \frac{1}{2}s_{max}$ and (*c*) $s = \frac{2}{3}s_{max}$.

Mach number is increasing, which is expected since the duct is converging. The agreement between direct and inverse calculation distributions is very good. It is believed that the small discrepancies observed near the exit region are partly due to the error accumulation of the geometry integrations and partly due to the inappropriate non-evolving zero Neumann boundary condition for t (actually the direct calculation indicates that the flow is evolving near the exit). Inverse and direct solver Mach number contours (solid and dashed lines respectively) on three cross-sections normal to the centreline at the locations $s = \frac{1}{3}s_{max}$, $\frac{1}{2}s_{max}$ and $\frac{2}{3}s_{max}$, s being the centreline arclength, are presented in figure 5. In spite of the fact that a 3-D interpolation procedure was used to produce these contours the reproduction is quite accurate.

5.2. *Axial converging–diverging nozzle test case*

The present inverse method has been applied to design an axial 3-D converging–diverging nozzle with prescribed (target) boundary velocity distribution. The prescribed velocity distribution, which is the same along all the wall streamlines, is presented in figure 6. The non-constant part of this distribution is described by a
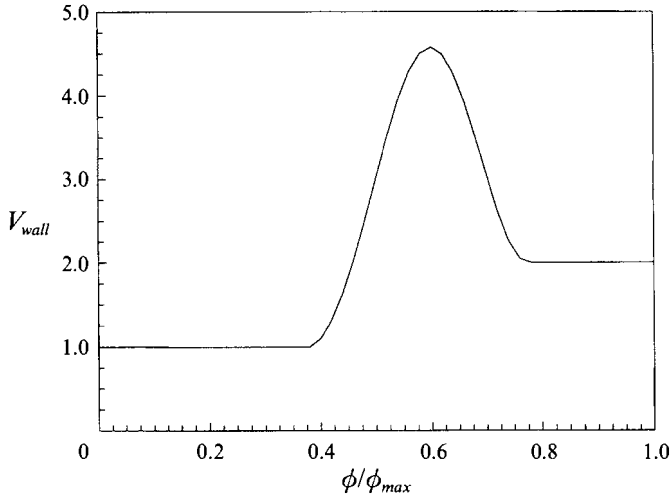
FIGURE 6. Target wall velocity distribution for the axial 3-D converging–diverging
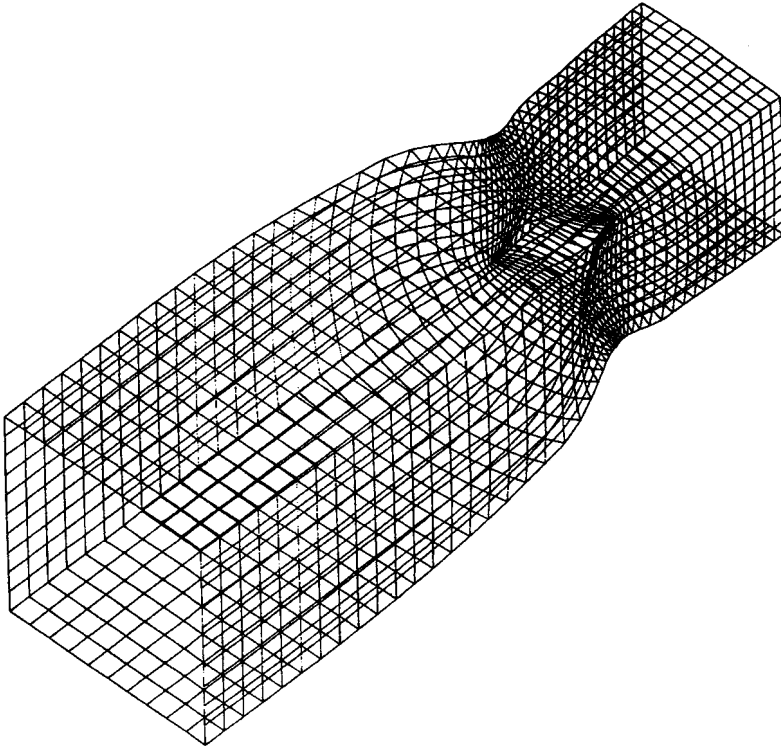nozzle test case.

FIGURE 7. Perspective view of the calculated axial 3-D converging–diverging nozzle.

sinusoidal function with linearly increasing amplitude. Uniform inlet and outlet
velocity distributions are specified. The inlet Mach number is set to 0.15.

It may be argued that this test case is a simple one since uniform, in the cross-flow
sense, wall boundary conditions correspond to axisymmetric (geometry) solution. It
should be realized, however, that such a (axisymmetric) solution is explicitly forbidden
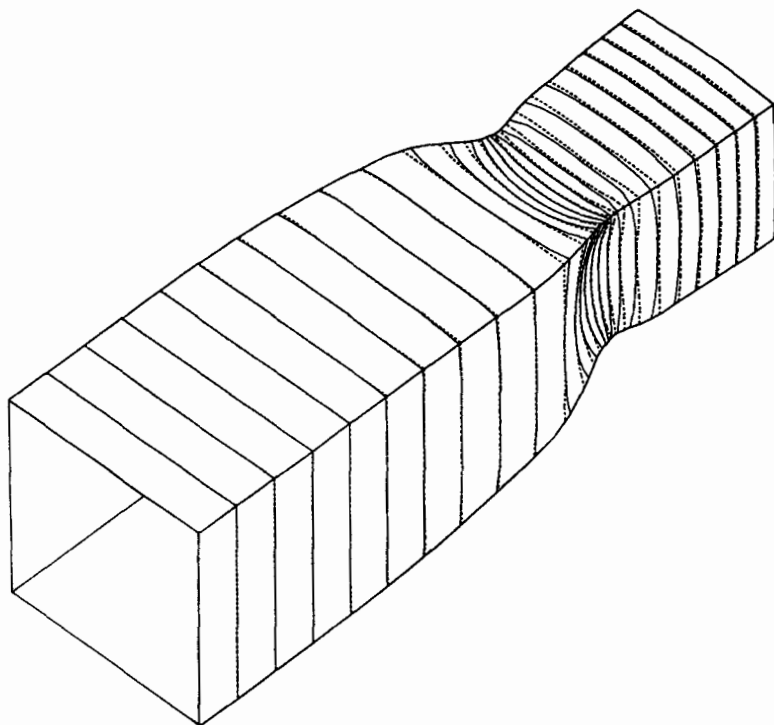
FIGURE 8. Potential lines of inverse (———) and direct (– – – –) method for two adjacent walls of the axial 3-D converging–diverging nozzle case ($\phi_{min} = 1$, $\Delta\phi = 2$).

since (*a*) the boundary conditions refer to both $\psi = $ const. and $\eta = $ const. family walls and (*b*) a square-sectioned inlet is assumed. This test case is definitely a hard test for the present inverse method.

Inverse calculation was carried out on a $51 \times 11 \times 11$ grid with $\Delta\phi = 1$, $\Delta\psi = 1$ and $\Delta\eta = 1$. A perspective view of the calculated nozzle, defined by the lateral-walls grid, is shown in figure 7. In the regions near the inlet and outlet, the nozzle has almost square cross-section. As the nozzle starts to converge, the wall surfaces become curved in a concave (outwards) manner. It seems that the flow solution tries to impose a 'near-axisymmetric' geometry, which (as was pointed out) is implied by the uniform, in the cross-flow sense, velocity boundary condition. In the throat region the walls of the nozzle are also curved, exhibiting however the opposite sense of curvature, i.e. concave inwards. As the flow approaches the exit it relaxes leading to a square cross-section. This is due not only to the uniform lateral and exit boundary conditions but also to the zero Neumann boundary condition for t.

The direct full-potential 3-D solver (Chaviaropoulos *et al.* 1988) employed for the reproduction procedure is applied using the grid produced by the inverse calculation. Inverse and direct solver results (solid and dashed lines respectively) for the potential function on two adjacent walls of the nozzle are compared in figure 8. The symmetry is very good and the agreement is quite satisfactory. The discrepancies observed near the edges, especially in the near-throat region are due to the high ϕ-values computed by the direct solver and associated with the local wall curvature. Part of the discrepancy is also due to the singular behaviour of the edge streamlines.

The streamwise distribution of the Mach number along the central streamline calculated with the inverse and direct methods is presented in figure 9. The Mach
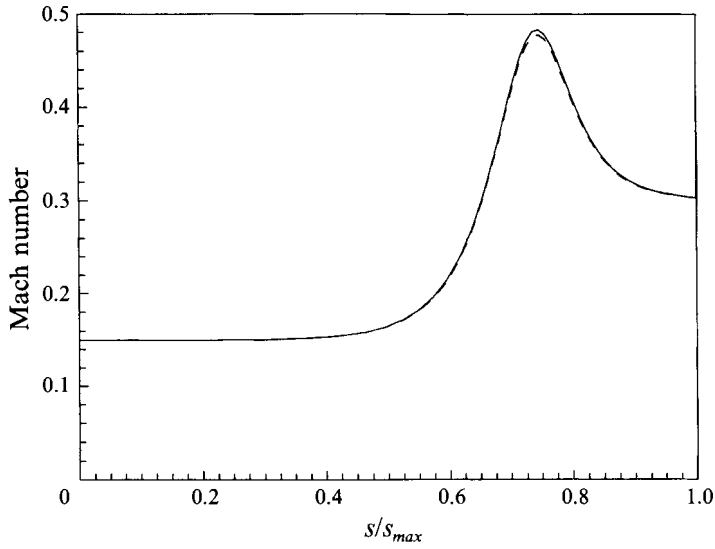
FIGURE 9. Mach number distributions of inverse (——) and direct (– – –) method along the centreline of the axial 3-D converging–diverging nozzle.
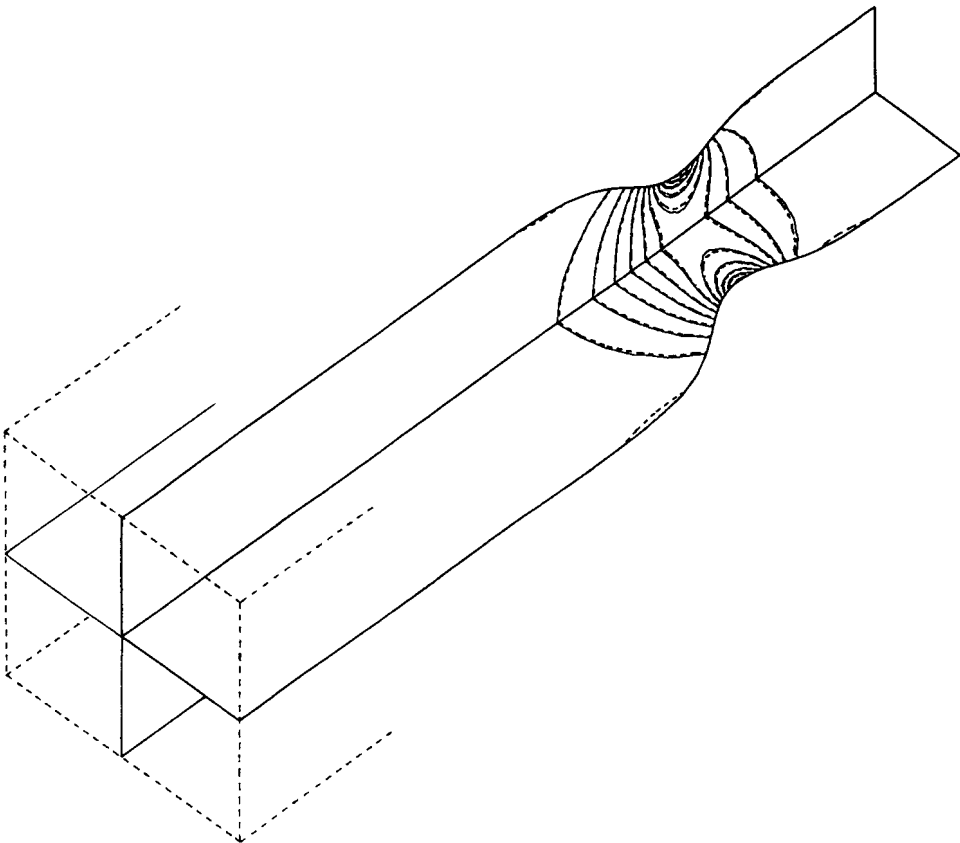

FIGURE 10. Mach number contours of inverse (——) and direct (– – –) method on the half of the central $\psi = $ const. and $\eta = $ const. stream surfaces of the axial 3-D converging–diverging nozzle ($M_{min} = 0.20$, $\Delta M = 0.05$).

number contours on the half of the central $\psi = $ const. and $\eta = $ const. stream surfaces of the inverse and direct solvers are compared in figure 10. The agreement is very good, indicating the reliability of the present method.

6. Conclusions

In the companion paper (Part 1) it was shown that the 3-D inverse potential target pressure problem can be formulated in terms of a potential function and two orthogonal stream functions, which are used as the independent variables (natural coordinates), and the velocity magnitude and the elementary streamtube aspect ratio which are considered to be the dependent variables. The numerical procedure developed for the solution of the 3-D inverse problem is presented and discussed.

An elliptic-type p.d.e. for the velocity magnitude and a second-order o.d.e. for the streamtube aspect ratio constitute the novel governing equations for the flow field. These equations are discretized using centred finite differencing on a staggered computational stencil, which increases the accuracy of the discretization in the near-boundary regions. The system of discrete equations is linearized and solved in a coupled manner employing an efficient preconditioned restarting GMRES(m) algorithm.

The geometry is determined after the flow solution is found, by integrating Frenet equations along the natural-coordinate grid lines. Frenet equations which form a coupled system of o.d.e.s for the covariant base are integrated using a Grank–Nicolson-type second-order-accurate space marching scheme.

The inverse method is validated for two internal flow reproduction test cases, concerning a double turning converging duct and an axial 3-D converging–diverging nozzle. The very good agreement between direct and inverse solver results indicates the reliability of the novel 3-D inverse method proposed.

REFERENCES

CHAVIAROPOULOS, P., DEDOUSSIS, V. & PAPAILIOU, K. D. 1995 On the 3-D inverse potential target pressure problem. Part 1. Theoretical aspects and method formulation. *J. Fluid Mech.* **282**, 131–146.

CHAVIAROPOULOS, P., GIANNAKOGLOU, K. & PAPAILIOU, K. D. 1988 A novel scalar-vector potential formulation for the numerical solution of 3D steady inviscid rotational flow problems. *AIAA J.* **26**, 1734–1739.

GIANNAKOGLOU, K., CHAVIAROPOULOS, P. & PAPAILIOU, K. D. 1988 Acceleration of standard full-potential and elliptic Euler solvers using preconditioned generalized minimal residual techniques. In *Flows in Non-rotating Turbomachinery Components* (ed. U. S. Rohatgi, A. Hamed & J. H. Kim). *ASME FED* Vol. 69, pp. 45–52.

RAO, K. V., STEGER, J. L. & PLETCHER, R. H. 1987 A three-dimensional dual potential procedure for inlets and indraft wind tunnels. *AIAA Paper* 87-0598.

SAAD, Y. & SCHULTZ, M. M. 1983 GMRES: A generalized minimal residual algorithm for solving nonsymmetric linear systems. *Department of Computer Science, Yale University Rep.* YALEU/DCS/RR-254.

STANITZ, J. D. 1980 General design method for three-dimensional potential flow fields. I-Theory. *NASA CR* 3288.

STANITZ, J. D. 1985 General design method for three-dimensional potential flow fields. II-Computer program DIN3D1 for simple unbranched ducts. *NASA CR* 3926.

YIH, C. S. 1957 Stream functions in three-dimensional flows. *Houille Blanche* **12**, 445–450.

ZEDAN, M. & SCHNEIDER, G. E. 1983 A three-dimensional modified strongly implicit procedure for heat conduction. *AIAA J.* **21**, 295–303.